Bioinspired Carbon/SnO2 Composite Anodes Prepared from a Photonic Hierarchical Structure for Lithium Batteries

Yao Li,[†] Qing Meng,[‡] Jun Ma,[§] Chengling Zhu,[†] Jingru Cui,[†] Zhixin Chen,[‡] Zaiping Guo,[‡] Tao Zhang,[†] Shenmin Zhu,*,[†] and Di Zhang*,[†]

[†]State Key Laboratory of Metal Matrix Composites, Shanghai Jiao Tong University, Shanghai 200240, China

[‡]School of Mechanical, Materials & Mechatronics Engineering, University of Wollongong, Wollongong, New South Wales 2522, Australia

[§]School of Advanced Manufacturing and Mechanical Engineering, University of South Australia, Adelaide, South Australia 5095, Australia

S *Supporting Information*
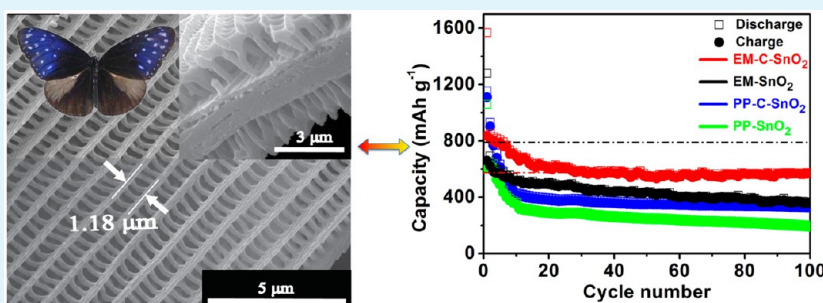
ABSTRACT: A carbon/SnO2 composite (C-SnO2) with hierarchical photonic structure was fabricated from the templates of butterfly wings. We have investigated for the first time its application as the anode material for lithium-ion batteries. It was demonstrated to have high reversible capacities, good cycling stability, and excellent high-rate discharge performance, as shown by a capacitance of $\sim$572 mAh g^{-1} after 100 cycles, 4.18 times that of commercial SnO2 powder (137 mAh g^{-1}); a far better recovery capability of 94.3% was observed after a step-increase and sudden-recovery current. An obvious synergistic effect was found between the porous, hierarchically photonic microstructure and the presence of carbon; the synergy guarantees an effective flow of electrolyte and a short diffusion length of lithium ions, provides considerable buffering room, and prevents aggregation of SnO2 particles in the discharge/charge processes. This nature-inspired strategy points out a new direction for the fabrication of alternative anode materials.

KEYWORDS: bioinspired material, 3D photonic structure, hierarchical, composite, anode material, lithium ion battery

1. INTRODUCTION

High-performance, lightweight energy storage devices are increasingly more important with portable electronic devices becoming smaller and smarter. Lithium-ion battery (LIB) is a competitive energy source owing to its high energy density, long cycle life, low self-discharge, as well as no "memory effect". Anode materials are among the major decisive factors for LIB performance. The limited theoretical capacity (372 mAh g^{-1}) of commercial graphite[1] has spurred intensive interest in the development of alternative materials. Featuring low cost and toxicity and a high theoretical capacity of 790 mAh g^{-1}, tin oxide (SnO2) is an ideal candidate.[2,3] Unfortunately, it has the disadvantage of rapid capacity fade due to pulverization caused by a rather large volume change of 250% when alloying with Li.[4,5]

To solve the problem, nanosized SnO2 particles have composited with a ductile matrix such as amorphous carbon;[6−8] this creates necessary buffering sites for the great volume change, acts as a carrier to prevent the nanoparticles aggregating, and provides these with electronic paths.[2,9] Meanwhile, structural design is proven effective in buffering volume change and preventing SnO2 from aggregation. SnO2 particles of various microstructures have been developed, including nanotubes,[6] nanosheets,[10] hollow spheres,[11] and nanowires,[12] all of which have demonstrated impressive performance as anode materials in Table 1.

The unique photonic structure has raised extensive interest in the development of high-performance electrode materials.[13] Stein is the first to produce carbon materials of inverse opal structures, making a 25% increase in capacity at $\sim$150 mA g^{-1} over spherical carbon; and this was attributed by the ordered, three-dimensional, well-interconnected pores and thin walls.[14]

Table 1. Performance of SnO$_2$ Anode Materials

structure	reference no.	cycling number	capacity after cycling (mAh g^{-1})	capacity retention/recovery ratio
nanotubes	6	200	540	92.5%
nanosheets	10	20	559	57%
hollow spheres	11	40	550	45.6%
nanowirees	12	50	773	68%

Since silicon is known for extraordinary theoretical capacity (4200 mA g^{-1}), Ozin synthesized silicon films of inverse-opal structures, demonstrating a capacity of 2374 mAh g^{-1} that retained 91.0% after 145 cycles.[15] While periodic structure may contribute to mechanical robustness, porous structure provides far more interface than solid structure between electrode and electrolyte, and this would shorten the diffusion length for lithium ions, resulting in a great many paths not only for ions but also for electrons. Hierarchical structure was an attractive option for high performance anode material. The large macroporous channels could provide an easily accessed pore system which facilitates electrolyte transportation and lithium ion diffusion,[16] and the micropores ensure high reversible capacity.[17] In addition, the thin walls of channels are conducive to the diffusion of Li ions and transportation of electrons to the interior of the porous carbons.[18] Therefore, a hypothesis made herein was that hierarchical photonic structure may provide an ideal path for the diffusion of electrolyte and ions, leading to high performance to electrode materials.[19−21] To the best of our knowledge, there are no reports on photonic crystals combined with hierarchical structure for LIB, due to the synthetic difficulty.[22]

Nature provides many examples of hierarchical photonic structures such as morpho-butterfly wing scales.[23−26] When a butterfly emerges from its chrysalis, its wings are very delicate, damp and crinkled. The butterfly then hangs upside down, and pumps body fluid through the intercollected channels of difference sizes in the wing scales, straightening and enlarging its wings; these channels form a network through which body liquid effectively flows through.

Inspired by nature, we in this work develop a novel carbon/SnO$_2$ composite featuring hierarchically photonic structure replicated from butterfly wings, investigate its performance as anode materials for LIB, and analyze the structure−property relations of the composite. The composite shows superior discharge capacity of 572 mAh g^{-1}, which is 4.18 times higher than the commercial SnO$_2$ particles (137 mAh g^{-1});[27] more importantly, the composite retains its capacity at 67.5% after 100 cycles. We then investigate the mechanisms.

2. EXPERIMENTAL SECTION

2.1. Synthesis of Composites. The synthesis process is described in Scheme 1. Euploeamulciber (EM) butterfly wings were pretreated and washed with anhydrous ethanol, and dried in air for 12 h. They were then immersed into tin precursor (a mixture of tin powder 5 g, nitric acid 36 mL, and deionized water 214 mL) for 10 h. These soaked butterfly wings were taken out, washed with deionized water, and dried overnight at room temperature under vacuum. After that, the impregnated butterfly wings were calcined under N$_2$ at 450 °C, to produce Euploeamulciber-carbon-SnO$_2$ (denoted EM-C-SnO$_2$), while the impregnated one calcined under air is EM-SnO$_2$. As a comparison, Papilioparis butterfly wings lacking photonic structures were used as a template. The samples prepared under N$_2$ and air were, respectively, Papilioparis-carbon-SnO$_2$ (PP-C-SnO$_2$) and PP-SnO$_2$. The wing scales treated under the same condition without impregnating with tin precursor are denoted as Papilioparis-carbon (PP-C) and Euploeamulciber-carbon (EM-C), respectively.

2.2. Characterization. Scanning electron microscopy (SEM) was performed on a JEOL JSM-6360LV field emission microscope at an accelerating voltage of 15 kV. Transmission electron microscopy (TEM) was carried out on a JEOL 2010 microscope at 200 kV. Nitrogen adsorption measurements were performed using an ASAP2020 volumetric adsorption analyzer at 77 K, after the samples had been degassed for 8 h in the degas port of the adsorption apparatus. The synthesized samples were characterized by X-ray diffraction (XRD) using a RigakuD/max2550VL/PC system operated at 35 kV and 200 mA with Cu Kα radiation (λ = 1.5406 Å), at a scan

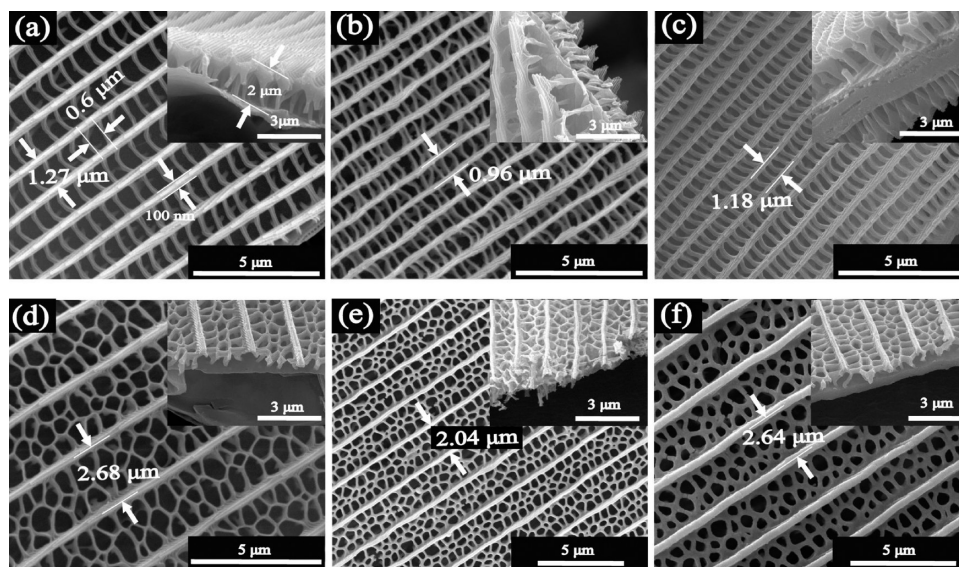**Scheme 1. Synthesis Process of a Bioinspired Carbon/SnO$_2$ Composite**
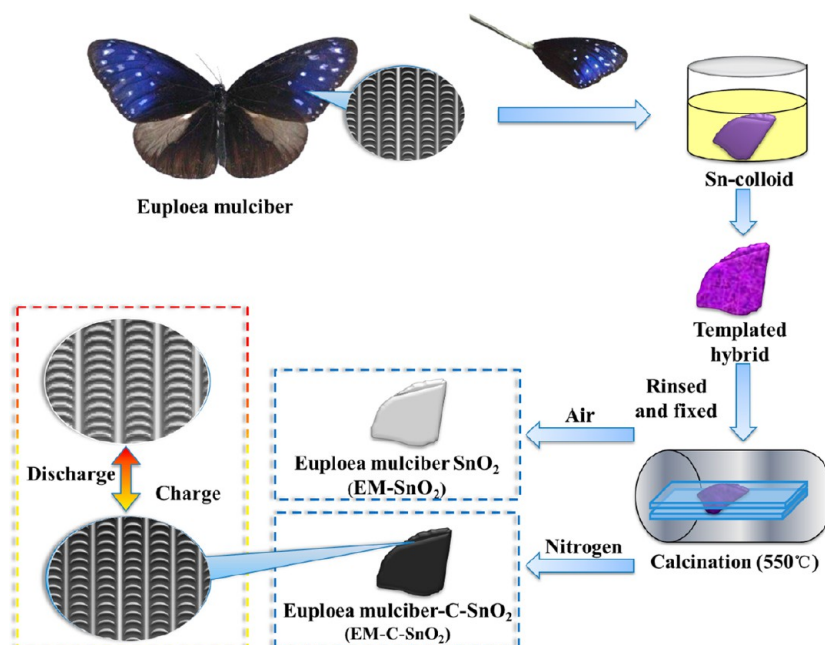
Figure 1. SEM and cross-section images (inset) of (a) original Euploeamulciber (EM), (b) EM-SnO$_2$, (c) EM-C-SnO$_2$, (d) original Papilioparis (PP), (e) PP-SnO$_2$, and (f) PP-C-SnO$_2$.

rate of 5° min^{-1} and a step size of 2θ = 0.050. Raman spectroscopy was performed on a Renishaw inVia Raman Microscope. Thermal gravimetric analysis (TGA) was conducted on a PE TGA-7 instrument with a heating rate of 20 °C min^{-1}.

2.3. Electrochemical Performance. Electrochemical experiments were carried out in a two-electrode Swagelok cell. The working electrodes were made by mixing the obtained composite with carbon black and binder (polyvinylidene fluoride, PVDF) at a mass ratio of 80:10:10. The mixture was then spread uniformly onto a copper foil cylinder with a diameter of 12 mm and dried in vacuum at 80 °C. The electrochemical cells used this active material as a working electrode, and Li foil as both counter electrode and reference electrode. The cells were assembled in an argon-filled glovebox (Mikrouna 1220/750). Metallic lithium foil was used as the counter electrode. The electrolyte was made of 1 M LiPF6 dissolved in the mixture of ethylene carbonate (EC) and diethylene carbonate (DEC) with a volume ratio of 1:1. Then, galvanostatic charge and discharge were carried out at a current density of 50 mA g^{-1} and cyclic voltammograms (CVs) were tested between 2.0 and 0 V at a scan rate of 0.2 mV s^{-1}. Electrochemical impedance spectra were measured by using a Chenhua CHI 660D electrochemical workstation with an AC voltage signal of 5 mV, in the frequency range between 100 kHz and 5 mHz. After 100 cycles, the cells were disassembled in the glovebox, and the working electrode was taken out and washed three times using dimethyl carbonate (DMC) solution. It was then prepared for SEM observation.

3. RESULTS AND DISCUSSION

Figure 1 shows secondary electron images of Euploeamulciber (EM) wing scales, Papilioparis (PP) wing scales, and their structure-replicated samples. EM wing scales demonstrate hierarchical, photonic structure (Figure 1a), where the space between two adjacent main ridges is ~1.27 μm, while the distance between two adjacent struts is 0.6 μm. Similar to many other butterflies and moths,[25,28] these scales consist of three levels. The upper ridges and ribs are supported by columnar pillars located at the bottom layer (Figure 1a insert). The ridges of 2 μm in height are decorated by lamellas, each of which is 100 nm thick. After replication, all of these features were topologically retained for both EM-SnO$_2$ (made in air, Figure 1b) and EM-C-SnO$_2$ (made in N$_2$, Figure 1c). The distances between two adjacent main ridges is ~0.96 μm for EM-SnO$_2$ (Figure 1b), while it is 1.18 μm for EM-C-SnO$_2$ (Figure 1c).

The shrinkage of EM-SnO$_2$ was measured as 24.4%, far greater than that of EM-C-SnO$_2$ (7.09%); this is explained by the loss of the carbon skeleton when calcination was conducted under air. Figure 1d contains morphologies of PP butterfly wing scale, where quasi-honeycomb-like structure is seen but unfortunately is not photonic structure (Figure 1d). Through replication with SnO$_2$, the distance between two adjacent ridges in PP-SnO$_2$ (Figure 1e) and PP-C-SnO$_2$ (Figure 1f) reduced 23.9% and 1.5%, with cross section views shown in the insets. In spite of shrinkage, the fine structures of scale ridges are exactly inherited from the template observed from the cross section images in Figure 1b and c inset. The periodic photonic structure of EM scales can release the stress concentration of the volume exchange during the discharge−charge process. We will discuss the implication of photonic structure for electrode performance in the following section.

These structures were further investigated by transmission electron microscopy (TEM) and high-resolution TEM (HR-TEM) in Figure 2. For EM-C-SnO$_2$, a seamless continuous shell at the contacting junction between the ridges and the scale bottom suggests that the sample retains the microstructural details of the original butterfly wing scales down to the nanoscale. High resolution TEM (HR-TEM) images reveal both EM-C-SnO$_2$ and EM-SnO$_2$ consisting of nanocrystallized SnO$_2$. As shown in Figure 2b and d, the spacing between two adjacent lattice planes is 3.34 Å,[29] corresponding to the d-spacing of (110) of rutile SnO$_2$.[30] Since the nanocrystal means shorter diffusion length and faster diffusion rate along the grain boundaries existing in nanomaterials, the as-prepared samples should provide desired buffering structure for the volume shakeup during the discharge−charge process.[31] The hierarchical photonic structure will be beneficial for reducing stresses associated with large volume changes during the insertion−removal process of lithium ion.[15] The four rings shown in the selected-area electron diffraction pattern (Figure 2b,d inset) could be indexed to (110), (101), (221), and (301) of rutile-type SnO$_2$. The microstructures of PP-C-SnO$_2$ and PP-SnO$_2$ replicas without photonic structures were also measured. A seamless continuous shell at the contacting junction between the ridges suggests that all the samples maintain the overall
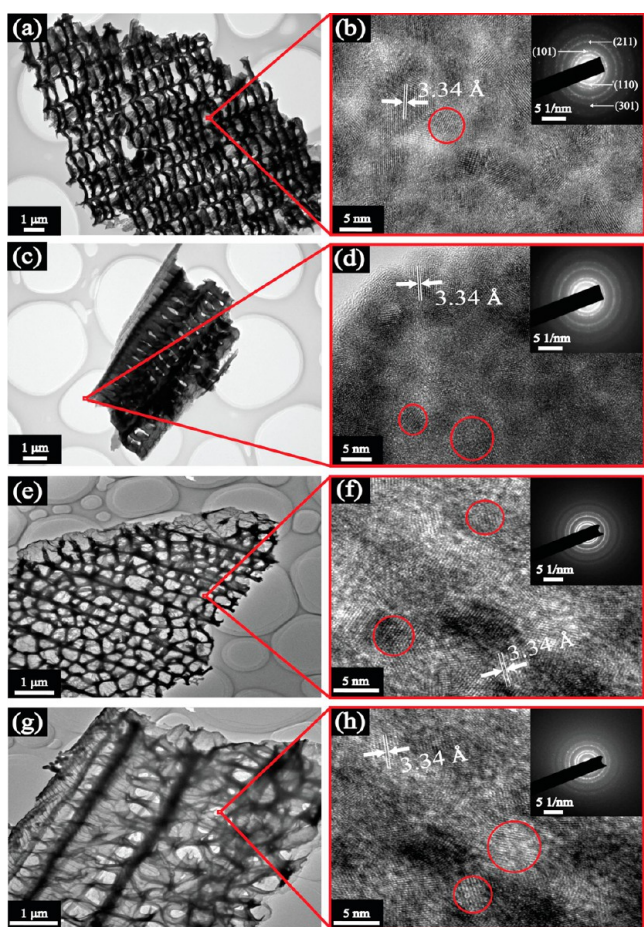
Figure 2. TEM micrographs and corresponding SAED patterns of EM-C-SnO₂ (a and b), EM-SnO₂ (c and d), PP-C-SnO₂ (e and f), and PP-SnO₂ (g and h).

scale morphology of the original butterfly wing (Figure 2e,g). The honeycomb structures down to nanoscale were confirmed directly by the images given in Figure 2e−h. The SnO$_2$ in PP-C-SnO$_2$ (Figure 2e) and PP-SnO$_2$ (Figure 2g) is rutile SnO$_2$, and so is EM-SnO$_2$ (Figure 2d). The pore structures were characterized by N$_2$ adsorption/desorption measurement (Figure S1).The specific surface areas of EM-C-SnO$_2$, EM-SnO$_2$, PP-C-SnO$_2$, and PP-SnO$_2$ were calculated to be around 36.0, 57.5, 37.1, and 42.2 m^2/g, respectively, according to the BET (Brunauer, Emmett, and Teller) analysis. Thus, carbon-containing samples (EM-C-SnO$_2$ and PP-C-SnO$_2$) possess a relatively lower surface area than carbon-free samples (EM-SnO$_2$ and PP-SnO$_2$). A hysteresis loop in the P/P_0 range of

0.4−1.0 was observed for all the samples, and the pore width was around 3.6 nm. That means these bioinspired samples maintained the hollow hierarchical microstructures of the original wing scales. Such a tubular interconnected network could provide efficient transport channels for the diffusion of electrolyte and lithium ion.

Figure 3a shows powder X-ray diffraction (XRD) patterns of EM-C-SnO$_2$, EM-SnO$_2$, PP-C-SnO$_2$, and PP-SnO$_2$. All the samples exhibit four major diffraction peaks located at 26.6°, 33.9°, 37.9°, and 51.8°, which are, respectively, indexed as the (110), (101), (200), and (211) of tetragonal rutile SnO$_2$ phase (Cassiterite, JCPDS card no. 41−1445). The broadened peaks indicate small crystallite size of SnO$_2$. Estimated from Scherrer's formula, the average crystallite sizes of all the samples are all below 6.6 nm, consistent with the TEM observations. It should be noted that the XRD patterns of carbon-containing samples (EM-C-SnO$_2$ and PP-C-SnO$_2$) are noisier than those of carbon-free samples (EM-SnO$_2$ and PP-SnO$_2$). This is probably due to the random dispersion of the diffraction effect from amorphous carbon.

The bioinspired composites were further characterized by Raman spectroscopy. In Figure 3b only one peak was detected at 635 cm^{-1} for both EM-SnO$_2$ and PP-SnO$_2$ prepared under air; this peak shows the characteristic of A$_{1g}$ symmetry of SnO$_2$. EM-C-SnO$_2$ and PP-C-SnO$_2$ prepared under N$_2$ contain carbon, with the peak of SnO$_2$ covered by the strong intensity of the carbon signal; two distinct new peaks at 1577 and 1353 cm^{-1} correspond to the G band (E$_{2g}$ phonon of C sp^2 atoms) and D bands (κ-point phonons of A$_{1g}$ symmetry) of carbon material.[32] G peak corresponds to the E$_{2g}$ phonon at the Brillouin zone center. The D peak is caused by the breathing modes of sp^2 rings and requires a defect for its activation; D peak intensity is not related to the number of graphene layers, but only to the amount of disorder. The intensity ratio I_D/I_G varies inversely with the size of the crystalline grains or interdefect distance. The I_D/I_G ratios of EM-C-SnO$_2$ and PP-C-SnO$_2$ are less than 1, which indicates the existence of ordered carbon.[33] That means that the conductivity of the replicas should be strengthened by carbon.

Figure S2 (SI) shows the thermogravimetric analysis (TGA) results for EM-C-SnO$_2$ and PP-C-SnO$_2$, and their SnO$_2$ percentages are estimated as ∼48.3% and 44.8%, respectively. Total 2% weight loss is detected in EM-SnO$_2$ and PP-SnO$_2$, indicating the full removal of the template (carbon) calcined in air.

The electrochemical properties of the bioinspired composite as anodes for lithium ion batteries were examined by cyclic voltammetry (CVs), as shown in Figure 4a and b and Figure S3 (SI) a and b. For all the samples, the difference between the
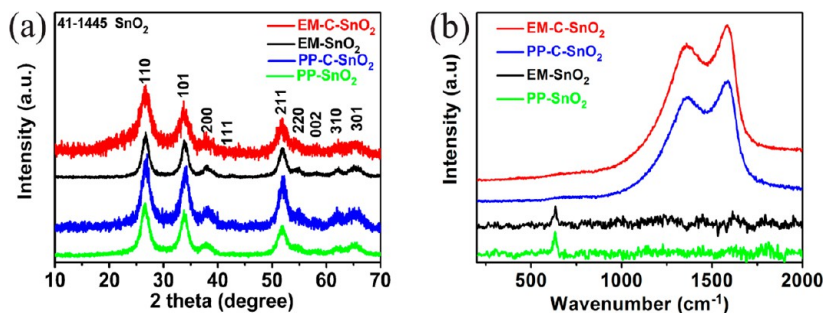

Figure 3. (a) XRD patterns and (b) Raman spectrum of EM-C-SnO₂, EM-SnO₂, PP-C-SnO₂, and PP-SnO₂.
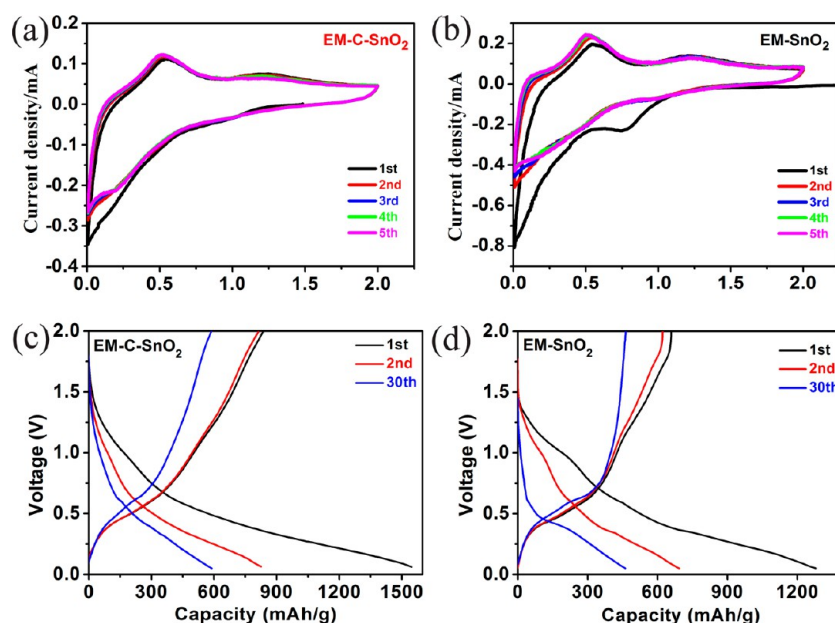
Figure 4. (a,b) Cyclic voltammograms and (c,d) discharge−charge profiles for the 1st, 2nd, and 30th cycle of lithium ion batteries with anodes made by (a,c) EM-C-SnO$_2$ and (b,d) EM-SnO$_2$.
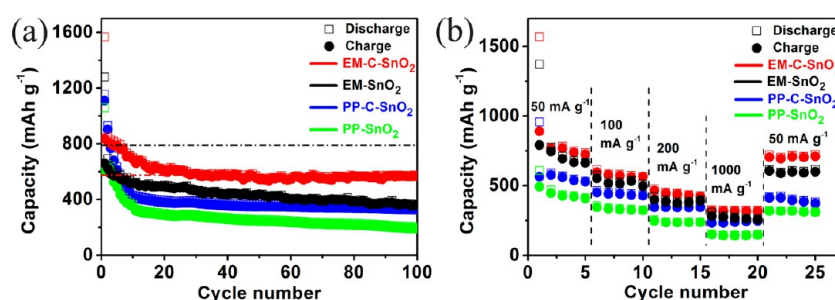

Figure 5. Capacities vs cycle number for EM-C-SnO$_2$, EM-SnO$_2$, PP-C-SnO$_2$, and PP-SnO$_2$ at (a) 50 mA g^{-1} and at (b) a different current density in a voltage window of 0.05−2.0 V.

first cycle and the following ones can be explained by the irreversible reactions occurred during the first cycle discharge process. In the first cycle solid-electrolyte interphase (SEI) films were formed over the surface of the anodes due to the reaction between anodes and electrolyte.[3] At the same time the reaction $SnO_2 + 4Li^+ + 4e^- \rightarrow Sn + 2Li_2O$ leads to an irreversible loss in capacity.[34] This phenomenon is well-known and unavoidable due to the decomposition of SnO$_2$ into Sn. These two factors yielded a peak at 0.75 V for EM-SnO$_2$ and PP-SnO$_2$ in the first cathodic scan, but it disappears in the subsequent cycles.[35] The carbon contained in EM-C-SnO$_2$ and PP-C-SnO$_2$ improved the electric conductivity of anode and prevented the aggregation of Sn nanoparticles, and thus the stability and the specific capacity of these two samples were much improved.

The subsequent cycles show similar CV profiles. The current peaks at ∼0.01 V for cathodic scan and 0.55 V for anodic scan can both be attributed to the reversible reaction $Sn + xLi^+ + xe^- \leftrightarrow Li_xSn$ ($x \leq 4.4$). In the cathodic scan, the 0.01 V current peak corresponds to the Li−Sn alloying and lithium intercalation of the anodes.[36] In the anodic sweep, the peak at 0.55 V shows the dealloying reaction of Li−Sn alloys. The anodic peak at 1.2 V and cathodic peak at 1.0 V both indicate partial reversibility of reaction between SnO$_2$ and Sn.[37]

The electrochemical performance of the bioinspired composites was further evaluated via galvanostatic discharge−charge cycling at a current density of 50 mA g^{-1} with voltage 0.05−2.0 V. Figure 4c,d shows typical discharge−charge profiles of EM-C-SnO$_2$ composite and EM-SnO$_2$ in the first two cycles and the 30th. The initial discharge specific capacity of EM-C-SnO$_2$ is 1567 mAh g^{-1} with a reversible specific capacity of 837 mAh g^{-1} while SnO$_2$ nanoparticles show 1279 mAh g^{-1} and 659 mAh g^{-1}. The initial columbic efficiency of EM-C-SnO$_2$ is 53.4%, which is slightly higher than EM-C-SnO$_2$ (51.5%) because of the inhibited effect of carbon on the irreversible reaction $SnO_2 + 4Li^+ + 4e^- \rightarrow Sn + 2Li_2O$. The large irreversible discharge capacity at the initial cycle of all four composites mainly resulted from the irreversible reduction of SnO$_2$ to Sn during the charging and discharging process. The reversible capacity of EM-C-SnO$_2$ maintains 73% (589 mAh g^{-1}) at the 30th cycle in comparison with 806 mAh g^{-1} at the second cycle; this performance is much better than that of EM-SnO$_2$ (68%). A similar phenomenon is observed in Figure S3c,d (SI). The capacity retention of PP-C-SnO$_2$ (61.1%) is better than PP-SnO$_2$ (57.7%) from the 2nd to 30th cycle. The marked capacity retention can be attributed to the buffering effect provided by SnO$_2$ nanoparticles, carbon component, and hierarchical periodic structure during the cycling process.
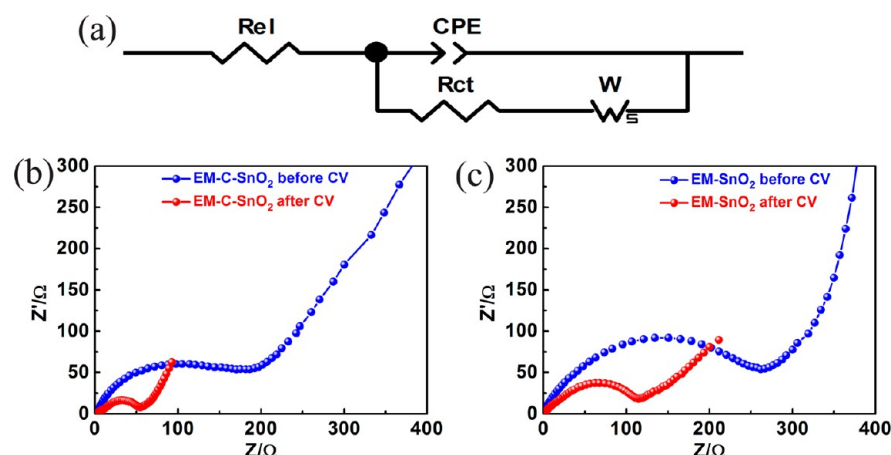
Figure 6. (a) Equivalent circuit of electrodes and Nyquist plots of (b) EM-C-SnO$_2$, (c) EM-SnO$_2$ obtained by applying a sine wave with an amplitude of 5.0 mV over the frequency range from 100 kHz to 0.01 Hz.

The cycling performances of EM-C-SnO$_2$, EM-SnO$_2$, PP-C-SnO$_2$, and PP-SnO$_2$ were compared at 50 mA g^{-1} in the voltage window of 5 mV to 2.0 V. As shown in Figure 5a, all these samples demonstrate high discharge capacities 1567, 1279, 1154, and 1058 mAh g^{-1} in the first cycle, respectively. The discharge capacity decreased to 848, 692, 929, and 650 mAh g^{-1} in the following cycles. The difference in the discharge capacity between the first and second cycles was attributed to the irreversible reactions as discussed early.

After 100 cycles, the four samples displayed three features. (i) The initial reversible capacity of EM-C-SnO$_2$ is significantly higher than that of PP-C-SnO$_2$; after 100 cycles the capacity maintains at ~572 mAh g^{-1}, 68.2% higher than PP-C-SnO$_2$ (~340 mAh g^{-1}). This dramatic difference is contributed from the hierarchically photonic structure (Figures 1 and 2) of EM-C-SnO$_2$; this unique structure not only guarantees the same diffusion distance of Li ion throughout the microstructure and the same volume swings during the discharge−charge process,[14,15] but provides an efficient exchange network of electrolyte. (ii) The reversible capacity of EM-C-SnO$_2$ is 58.0% higher than that of EM-SnO$_2$ (~362 mAh g^{-1}), even though they have similar photonic structures. This difference contributed to the enhanced electric conductivity by carbon. (iii) The reversible capacity of PP-SnO$_2$ was at ~210 mAh g^{-1}, 1.53 times that of commercial SnO$_2$ powder (~137 mAh g^{-1}).[27] This is likely due to the bioinspired microstructures consisting of nanosized SnO$_2$ particles, which provides buffering space for the large volume change of anode material and prevents the aggregation of Li−Sn alloy during the cycling process. It should be noted that the high reversible capacity ~572 mAh g^{-1} after 100 cycles exhibited by EM-C-SnO$_2$ is 4.18 times that of commercial SnO$_2$ powder reported (137 mAh g^{-1}).[27] The reason could be that (i) the accessible, interconnected, porous structure ensures an effective flow of electrolyte, (ii) periodic yet hierarchically photonic microstructure (Figures 1 and 2) not only shortens the Li diffusion, but provides considerable buffering room for the high volume change of SnO$_2$, and (iii) carbon matrix provides electronic paths and prevents SnO$_2$ particles from aggregating.

To further investigate the contribution of structures and SnO$_2$ components on the properties, cycling performance of EM-C and PP-C were measured shown in Figure S4. Both EM-C and PP-C showed considerable stability during the cycle process. A reversible capacity of 256 mAh g^{-1} for EM-C was

performed after 100 cycles, which was 45% improvement compared with that of PP-C (176 mAh g^{-1}). It indicated that the hierarchical photonic structure of EM contributed a great deal to the high performance of EM-C.

The current rate performances of samples EM-C-SnO$_2$, EM-SnO$_2$, PP-C-SnO$_2$, and PP-SnO$_2$ were measured as shown in Figure 5b. During the first five cycles, EM-C-SnO$_2$ shows a capacity of ~795 mAh g^{-1} at 50 mA g^{-1}. When the current rate increases stepwise up to 1000 mA g^{-1}, EM-C-SnO$_2$ could still deliver a stable capacity of ~329 mAh g^{-1}. When the current rate reduced to 50 mA g^{-1}, a stable high capacity of ~750 mAh g^{-1} was obtained. The discharge capacity of EM-C-SnO$_2$ could recover 94.3% after this process. In comparison, the discharge capacity of PP-C-SnO$_2$ maintains only ~72.0% at first five cycles. Obviously, the samples with periodic structure showed better rate performance than the samples with aperiodic structure during the rate cycling process.

The reversible capacity of EM-C-SnO$_2$ was significantly better than the that of the rest. This is presumably because of the synergetic effects of the bioinspired hollow periodic structure, SnO$_2$ nanoparticles, and the presence of carbon in the composite. First, the bioinspired hollow periodic structure not only guarantees the same diffusion distance of Li ion and the same volume swings during discharge−charge process, but also provides an efficient exchange network of electrolyte. Second, SnO$_2$ nanoparticles provide buffering space for the great volume change of anode material.[30] Third, the presence of carbon in the composite enhanced the electric conductivity of composite, and prevents the aggregation of Li−Sn alloy during the discharge−charge process.

In order to verify the electrochemical performance of EM-C-SnO$_2$ in comparison with that of EM-SnO$_2$, PP-C-SnO$_2$, and PP-SnO$_2$, electrochemical impedance spectroscopy measurements were carried out. As shown in Figure S5 (SI), the Nyquist plots of all composites after and before 5 cycles show a semicircle in the high frequency range and a straight line in the low frequency. The equivalent circuit of the electrodes is shown in Figure 6a where Rel, CPE, Rct, and W are denoted as solution resistance, double layer capacitance, charge-transfer resistance, and Warburg impedance, respectively. The charge-transfer resistance (R_{ct}) of the EM-C-SnO$_2$ was calculated to be ~56 Ω after 5 cycles (Figure 6b), similar to that of PP-C-SnO$_2$ (~58 Ω) (SI Figure S3a); these values are much lower than those of EM-SnO$_2$ (Figure 6c) and PP-SnO$_2$ (SI Figure S4b)

electrode (117 and 95). The low resistance is attributed to the presence of carbon in the composites leading to good electrical conductivity.

To understand the excellent electrochemical performance of the composite of unique photonic structure, the morphology and microstructure variation of the EM-C-SnO$_2$, EM-SnO$_2$, PP-C-SnO$_2$, and PP-SnO$_2$ after 100 discharge−charge cycles were examined using SEM (Figures 7a−h and S2a−h). It is obviously
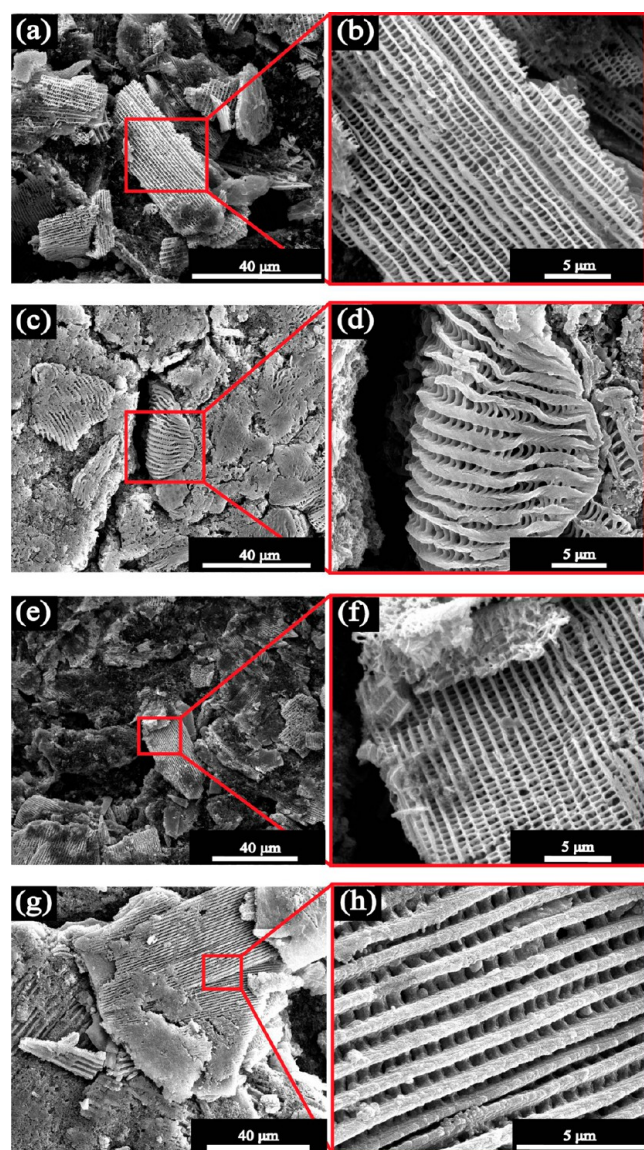

Figure 7. SEM images for EM-C-SnO$_2$ (a,b) before and (c,d) after 100 discharge/charge cycles, and for EM-SnO$_2$ (e,f) before and (g,h) after 100 discharge/charge cycles.

demonstrated that the microstructure of EM-C-SnO$_2$ was maintained the best (Figure 7c,d). The fine structure of EM-C-SnO$_2$ appears slightly thickened and coarsened through the cycling (Figure 7c,d) (Figure 1c), corresponding to the excellent cycling performance in Figure 5a. After 100 discharge−charge cycles, the four samples displays three features: first, the microstructure of EM-C-SnO$_2$ (Figure 7c,d) remains better than PP-C-SnO$_2$ (Figure 8c,d) because of lower stress concentration of periodic photonic structure during the cycling process; second, in comparison with EM-
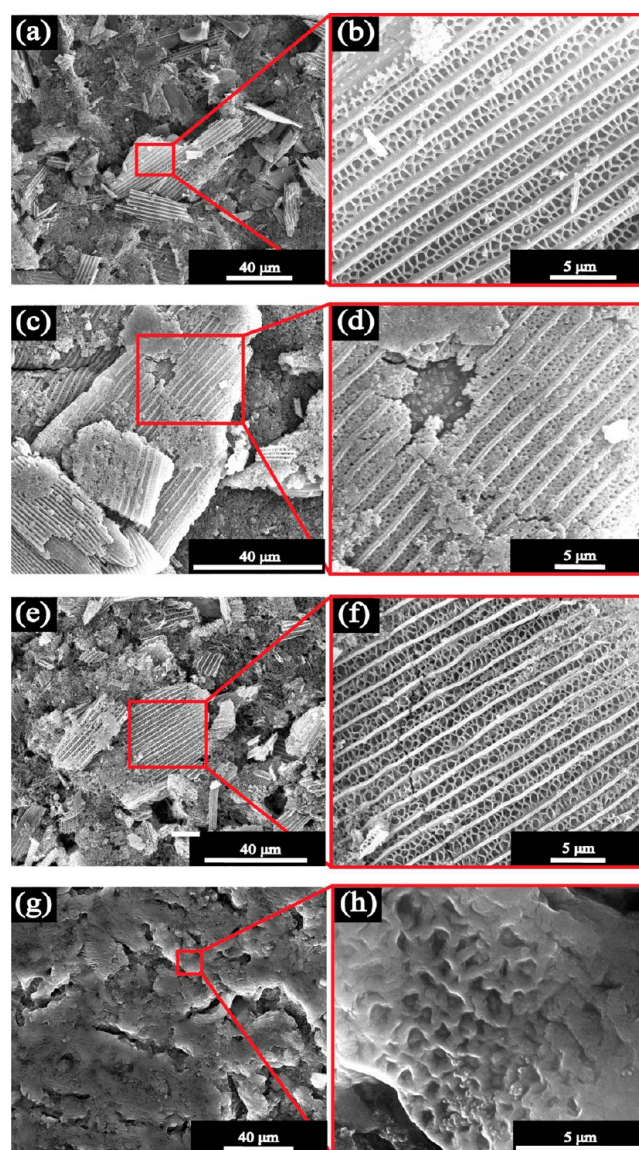

Figure 8. SEM images for PP-C-SnO$_2$ (a,b) before and (c,d) after 100 discharge/charge cycles, and for PP-SnO$_2$ (e,f) before and (g,h) after 100 discharge/charge cycles.

SnO$_2$ (Figure 7g,h), no obvious cracks can be seen for EM-C-SnO$_2$ (Figure 7c,d) because of the carbon-support (Figure 7g,h). Third, the microstructure of PP-SnO$_2$ (Figure 8g,h) displayed obviously more damage through the cycling due to the stress concentration of nonperiodic photonic structure and the absence of carbon support. The observation explains the electrochemical performance of these composites.

4. CONCLUSION

In summary, a bioinspired SnO$_2$/carbon composite with hierarchically photonic structure was fabricated as the anode material for lithium batteries. When calcined under N$_2$ atmosphere, bioinspired EM-C-SnO$_2$ was obtained which has a photonic structure. The composite exhibited excellent reversible capacity and cycling consistency. A discharge capacity of ∼572 mAh g^{-1} after 100 cycles was maintained, an increase of 68.2% over the PP-C-SnO$_2$ with a honeycomb structure. When subject to step increasing current and sudden recovery current, a far better recovery capability of 94.3% was observed

for EM-C-SnO$_2$ than PP-C-SnO$_2$. The excellent performance is attributed to the synergistic effect of SnO$_2$ nanoparticles, carbon matrix, photonic structure, and efficient hierarchical tunnel network inherited from the biotemplate. This fundamental research and the promising properties demonstrate that this bioinspired hierarchical photonic structure is not only promising for high rate and stable anode material for lithium ion batteries, but also can brighten the way for the development of novel materials for LIBs.

ASSOCIATED CONTENT

Supporting Information

TGA curves of EM-C-SnO$_2$, EM-SnO$_2$, PP-C-SnO$_2$, and PP-SnO$_2$; cyclic voltammograms and discharge−charge profiles; capacities vs cycle number of PP-C-SnO$_2$ and PP-SnO$_2$; SEM images of EM-C-SnO$_2$ and EM-SnO$_2$ anode before and after 100 discharge/charge cycles. The Supporting Information is available free of charge on the ACS Publications website at DOI: 10.1021/acsami.5b02774.

AUTHOR INFORMATION

Corresponding Authors

*E-mail: smzhu@sjtu.edu.cn. Tel/Fax: +86-21-34203927.
*E-mail: zhangdi@sjtu.edu.cn.

Notes

The authors declare no competing financial interest.

ACKNOWLEDGMENTS

REFERENCES

(1) Hu, Y. S.; Adelhelm, P.; Smarsly, B. M.; Hore, S.; Antonietti, M.; Maier, J. Synthesis of Hierarchically Porous Carbon Monoliths with Highly Ordered Microstructure and Their Application in Rechargeable Lithium Batteries with High-rate Capability. *Adv. Funct. Mater.* **2007**, *17*, 1873−1878.

(2) Li, Y.; Zhu, S.; Liu, Q.; Gu, J.; Guo, Z.; Chen, Z.; Feng, C.; Zhang, D.; Moon, W.-J. Carbon-coated SnO$_2$@C with Hierarchically Porous Structures and Graphite Layers inside for a High-performance Lithium-ion Battery. *J. Mater. Chem.* **2012**, *22*, 2766−2773.

(3) Lou, X. W.; Chen, J. S.; Chen, P.; Archer, L. A. One-pot Synthesis of Carbon-coated SnO$_2$ Nanocolloids with Improved Reversible Lithium Storage Properties. *Chem. Mater.* **2009**, *21*, 2868−2874.

(4) Larcher, D.; Beattie, S.; Morcrette, M.; Edstrom, K.; Jumas, J. C.; Tarascon, J. M. Recent Findings and Prospects in the Field of Pure Metals as Negative Electrodes for Li-ion Batteries. *J. Mater. Chem.* **2007**, *17*, 3759−3772.

(5) Tarascon, J. M.; Armand, M. Issues and Challenges Facing Rechargeable Lithium Batteries. *Nature* **2001**, *414*, 359−367.

(6) Wang, Y.; Zeng, H. C.; Lee, J. Y. Highly Reversible Lithium Storage in Porous SnO$_2$ Nanotubes with Coaxially Grown Carbon Nanotube Overlayers. *Adv. Mater.* **2006**, *18*, 645−649.

(7) Yuan, L.; Konstantinov, K.; Wang, G. X.; Liu, H. K.; Dou, S. X. Nano-structured SnO$_2$-carbon Composites Obtained by in situ Spray Pyrolysis Method as Anodes in Lithium Batteries. *J. Power Sources* **2005**, *146*, 180−184.

(8) Chen, J. S.; Cheah, Y. L.; Chen, Y. T.; Jayaprakash, N.; Madhavi, S.; Yang, Y. H.; Lou, X. W. SnO$_2$ Nanoparticles with Controlled Carbon Nanocoating as High-capacity Anode Materials for Lithium-ion Batteries. *J. Phys. Chem. C* **2009**, *113*, 20504−20508.

(9) Han, F.; Li, W.-C.; Li, M.-R.; Lu, A.-H. Fabrication of Superior-performance SnO$_2$@C Composites for Lithium-ion Anodes Using Tubular Mesoporous Carbon with Thin Carbon Walls and High Pore Volume. *J. Mater. Chem.* **2012**, *22*, 9645−9651.

(10) Wang, C.; Zhou, Y.; Ge, M.; Xu, X.; Zhang, Z.; Jiang, J. Z. Large-scale Synthesis of SnO$_2$ Nanosheets with High Lithium Storage Capacity. *J. Am. Chem. Soc.* **2009**, *132*, 46−47.

(11) Lou, X. W.; Wang, Y.; Yuan, C.; Lee, J. Y.; Archer, L. A. Template-free Synthesis of SnO$_2$ Hollow Nanostructures with High Lithium Storage Capacity. *Adv. Mater.* **2006**, *18*, 2325−2329.

(12) Kim, H.; Cho, J. Hard Templating Synthesis of Mesoporous and Nanowire SnO$_2$ Lithium Battery Anode Materials. *J. Mater. Chem.* **2008**, *18*, 771−775.

(13) Magasinski, A.; Dixon, P.; Hertzberg, B.; Kvit, A.; Ayala, J.; Yushin, G. High-performance Lithium-ion Anodes Using a Hierarchical Bottom-up Approach. *Nat. Mater.* **2010**, *9*, 353−358.

(14) Lee, K. T.; Lytle, J. C.; Ergang, N. S.; Oh, S. M.; Stein, A. Synthesis and Rate Performance of Monolithic Macroporous Carbon Electrodes for Lithium-ion Secondary Batteries. *Adv. Funct. Mater.* **2005**, *15*, 547−556.

(15) Esmanski, A.; Ozin, G. A. Silicon Inverse-opal-based Macroporous Materials as Negative Electrodes for Lithium Ion Batteries. *Adv. Funct. Mater.* **2009**, *19*, 1999−2010.

(16) Fu, L. J.; Yang, L. C.; Shi, Y.; Wang, B.; Wu, Y. P. Synthesis of Carbon Coated Nanoporous Microcomposite and its Rate Capability for Lithium Ion Battery. *Microporous Mesoporous Mater.* **2009**, *117*, 515−518.

(17) Wu, Y.-P.; Wan, C.-R.; Jiang, C. Y.; Fang, S. B.; Jiang, Y. Y. Mechanism of Lithium Storage in Low Temperature Carbon. *Carbon* **1999**, *37*, 1901−1908.

(18) Zhang, F.; Wang, K.-X.; Li, G.-D.; Chen, J.-S. Hierarchical Porous Carbon Derived from Rice Straw for Lithium Ion Batteries with High-rate Performance. *Electrochem. Commun.* **2009**, *11*, 130−133.

(19) Jeong, J.-M.; Choi, B. G.; Lee, S. C.; Lee, K. G.; Chang, S.-J.; Han, Y.-K.; Lee, Y. B.; Lee, H. U.; Kwon, S.; Lee, G.; Lee, C.-S.; Huh, Y. S. Hierarchical Hollow Spheres of Fe$_2$O$_3$@polyaniline for Lithium Ion Battery Anodes. *Adv. Mater.* **2013**, *25*, 6250−6255.

(20) Ma, Y.; Fang, C.; Ding, B.; Ji, G.; Lee, J. Y. Fe-doped Mn$_x$O$_y$ with Hierarchical Porosity as a High-performance Lithium-ion Battery Anode. *Adv. Mater.* **2013**, *25*, 4646−4652.

(21) Xiong, S.; Bai, Z.; Ju, Z.; Guo, C.; Tang, B.; Qian, Y. Direct Large-scale Synthesis of 3D Hierarchical Mesoporous NiO Microspheres as High-performance Anode Materials for Lithium Ion Batteries. *Nanoscale* **2014**, *6*, 3268−3273.

(22) Campbell, M.; Sharp, D. N.; Harrison, M. T.; Denning, R. G.; Turberfield, A. J. Fabrication of Photonic Crystals for the Visible Spectrum by Holographic Lithography. *Nature* **2000**, *404*, 53−56.

(23) Parker, A. R.; Townley, H. E. Biomimetics of Pphotonic Nanostructures. *Nat. Nanotechnol.* **2007**, *2*, 347−353.

(24) Huang, J.; Wang, X.; Wang, Z. L. Controlled Replication of Butterfly Wings for Achieving Tunable Photonic Properties. *Nano Lett.* **2006**, *6*, 2325−2331.

(25) Vukusic, P.; Sambles, J. R. Photonic Structures in Biology. *Nature* **2003**, *424*, 852−855.

(26) Zhang, W.; Zhang, D.; Fan, T.; Gu, J.; Ding, J.; Wang, H.; Guo, Q.; Ogawa, H. Novel Photoanode Structure Templated from Butterfly Wing Scales. *Chem. Mater.* **2008**, *21*, 33−40.

(27) Zhang, L. S.; Jiang, L. Y.; Yan, H. J.; Wang, W. D.; Wang, W.; Song, W. G.; Guo, Y. G.; Wan, L.-J. Mono Dispersed SnO$_2$ Nanoparticles on Both Sides of Single Layer Graphene Sheets as Anode Materials in Li-ion Batteries. *J. Mater. Chem.* **2010**, *20*, 5462−5467.

(28) Saranathan, V.; Osuji, C. O.; Mochrie, S. G. J.; Noh, H.; Narayanan, S.; Sandy, A.; Dufresne, E. R.; Prum, R. O. Structure, Function, and Self-assembly of Single Network Gyroid (I4132) Photonic Crystals in Butterfly Wing Scales. *Proc. Natl. Acad. Sci. U.S.A.* **2010**, *107*, 11676−11681.

(29) Wang, X.; Zhou, X.; Yao, K.; Zhang, J.; Liu, Z. A SnO_2/graphene Composite as a High Stability Electrode for Lithium Ion Batteries. *Carbon* **2011**, *49*, 133−139.

(30) Wen, Z.; Wang, Q.; Zhang, Q.; Li, J. In situ Growth of Mesoporous SnO_2 on Multiwalled Carbon Nanotubes: a Novel Composite with Porous-tube Structure as Anode For Lithium Batteries. *Adv. Funct. Mater.* **2007**, *17*, 2772−2778.

(31) Meduri, P.; Pendyala, C.; Kumar, V.; Sumanasekera, G. U.; Sunkara, M. K. Hybrid tin Oxide Nanowires as Stable and High Capacity Anodes for Li-ion Batteries. *Nano Lett.* **2009**, *9*, 612−616.

(32) Tuinstra, F.; Koenig, J. L. Raman Spectrum of Graphite. *J. Chem. Phys.* **1970**, *53*, 1126−1130.

(33) Cuesta, A.; Dhamelincourt, P.; Laureyns, J.; Martínez-Alonso, A.; Tascón, J. M. D. Raman Microprobe Studies on Carbon Materials. *Carbon* **1994**, *32*, 1523−1532.

(34) Park, M.-S.; Wang, G.-X.; Kang, Y.-M.; Wexler, D.; Dou, S.-X.; Liu, H.-K. Preparation and Electrochemical Properties of SnO_2 Nanowires for Application in Lithium-ion Batteries. *Angew. Chem., Int. Ed.* **2007**, *46*, 750−753.

(35) Li, X.; Meng, X.; Liu, J.; Geng, D.; Zhang, Y.; Banis, M. N.; Li, Y.; Yang, J.; Li, R.; Sun, X.; Cai, M.; Verbrugge, M. W. Tin Oxide with Controlled Morphology and Crystallinity by Atomic Layer Deposition onto Graphene Nanosheets for Enhanced Lithium Storage. *Adv. Funct. Mater.* **2012**, *22*, 1647−1654.

(36) Chang, C.-C.; Liu, S.-J.; Wu, J.-J.; Yang, C.-H. Nano-tin Oxide/tin Particles on a Graphite Surface as an Anode Material for Lithium-ion Batteries. *J. Phys. Chem. C* **2007**, *111*, 16423−16427.

(37) Lou, X. W.; Chen, J. S.; Chen, P.; Archer, L. A. One-Pot Synthesis of Carbon-Coated SnO_2 Nanocolloids with Improved Reversible Lithium Storage Properties. *Chem. Mater.* **2009**, *21*, 2868−2874.